Role of convergence obliquity and inheritance on sliver tectonics: Insights from 3-D subduction experiments

Rodrigo Suárez, Benjamin Guillaume, Joseph Martinod, Matías Ghiglione, Christian Sue, Jean-Jacques Kermarrec

Journal Pre-proof

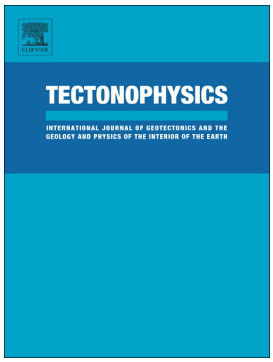

Role of convergence obliquity and inheritance on sliver tectonics: Insights from 3-D subduction experiments

Rodrigo J. Suárez, Benjamin Guillaume, Joseph Martinod, Matías C. Ghiglione, Christian Sue, Jean-Jacques Kermarrec

PII: S0040-1951(22)00377-8

DOI: https://doi.org/10.1016/j.tecto.2022.229583

Reference: TECTO 229583

To appear in: *Tectonophysics*

Received date: 5 April 2022

Revised date: 10 September 2022

Accepted date: 11 September 2022

Please cite this article as: R.J. Suárez, B. Guillaume, J. Martinod, et al., Role of convergence obliquity and inheritance on sliver tectonics: Insights from 3-D subduction experiments, *Tectonophysics* (2022), https://doi.org/10.1016/j.tecto.2022.229583

ROLE OF CONVERGENCE OBLIQUITY AND INHERITANCE ON SLIVER TECTONICS: INSIGHTS FROM 3-D SUBDUCTION EXPERIMENTS

Rodrigo J. Suárez[a,b,*], Benjamin Guillaume[c], Joseph Martinod[d], Matías C. Ghiglione[a], Christian Sue[d,e], Jean-Jacques Kermarrec[c]

[a]Instituto de Estudios Andinos IDEAN (Universidad de Buenos Aires - CONICET), Buenos Aires, Argentina.

[b]Instituto de Investigación en Paleobiología y Geología (Universidad Nacional de Río Negro - CONICET), General Roca, Argentina

[c]Université de Rennes, CNRS, Géosciences Rennes, UMR 6118, Rennes, France

[d]ISTerre, Université Grenoble Alpes, Université Savoie Mont-Blanc, 73376 Le Bourget du Lac cedex, France

[e]Université de Franche-Comté, Besançon, France

***Corresponding author:** Rodrigo Javier Suárez. Now at Instituto de Investigación en Paleobiología y Geología (Universidad Nacional de Río Negro - CONICET), General Roca, Argentina. Personal e-mail: rodrigo_s_37@hotmail.com;

Abstract. The subduction dynamics and deformation style in the framework of subduction zones have been classically understood under a vision of trench-orthogonal plate convergence. We perform 3-D upper mantle-scale analog models to further understand the dynamics of subduction systems and overriding plate strain distribution under varying convergence angles and in the presence or absence of intraplate inherited weak zones. The laboratory experiments show that whatever the obliquity of convergence, the subduction dynamics is largely influenced by the interaction of the slab with the 660 km discontinuity. The slab geometry alternates between stages of slab shallowing and steepening, which are accompanied by alternating periods of shortening and stretching (or moderate shortening) of the overriding plate, respectively. As convergence departs from being orthogonal and in the absence of an intraplate inherited weak zone, strain within the overriding plate shifts from pure shear to sub-simple shear. When a lithospheric-scale weak zone is introduced along the forearc-arc interface and under trench-oblique convergence, the strain is partitioned and the forearc develops sliver motion - and independent deformation - from the rest of the overriding plate. The forearc evolution is characterized by a three-step history: (i) detachment and oceanward motion, (ii) advancing motion toward the continent, and, (iii) accretion that can ultimately lead to underthrusting of the forearc. Decreasing slab dip increases the interplate force, resulting in larger stresses applied on the intraplate fault separating the forearc sliver from the continent. Hence, models show that because larger compression increases the coupling between the forearc and the plate, it does not favor sliver motion.

Key-words. Laboratory experiments; Subduction dynamics; Upper plate strain; Oblique convergence; Sliver motion; Orogenic systems;

1. INTRODUCTION

Subduction zones are usually pictured as trench-orthogonal plate convergence zones, despite parametric studies of subduction zones have shown that trench-oblique plate convergence is the most common regime along convergent plate margins worldwide (Kimura, 1986; Jarrard 1986a, 1986b; Philippon and Corti, 2016; Balázs et al. 2021). Philippon and Corti (2016) demonstrate that trench-orthogonal convergence (at 80-90°) only represents 10% of cases. While modeling subduction zones under trench-orthogonal convergence turns out fundamental to illustrate the overall subduction dynamics and forces at work, an understanding of the impact of variations of obliquity convergence is fundamental for assessing strain distribution across the upper plate (Chemenda et al. 2000; Balázs et al. 2021).

Trench-oblique plate convergence can produce strain partitioning, i.e., the deformation (*sensu lato*) within the overriding plate is heterogeneously distributed into trench-parallel strike-slip or simple shear and trench-perpendicular shortening/extension (coaxial strain) (Tikkof and Teyssier, 1994; Teyssier et al. 1995; Fossen and Tikoff, 1998; Chemenda et al., 2000; Cooke et al. 2020). In some cases, favored by a trench-parallel component of convergence (*y*-component) larger than the trench-normal component (*x*-component), a forearc "sliver" can develop (Fitch, 1972; Jarrard, 1986b; Kimura, 1986; McCaffrey, 1992; Beck, 1991; Beck et al. 1993; Teyssier et al. 1995), i.e., a piece of overriding plate located between the trench and a margin parallel, strike-slip fault (e.g., Haq and Davies, 2010). A pioneer work performed by Fitch (1972) showed that earthquakes focal mechanisms in the western Pacific island arcs were characterized by trench-parallel slip, evidencing that in subduction systems undergoing trench-oblique convergence, the trench-parallel component is taken up by trench-parallel strike-slip faults running alongside the

volcanic arc. Other studies showed that the sliver motion may be favored by: (i) a high-angle of trench-oblique convergence, (ii) a low slab dip (i.e., high-mechanical coupling), and (iii) the softening of the magmatic arc by thermal effects (Beck, 1983, 1991). Chemenda et al. (2000) using laboratory models of trench-oblique convergence proposed that strain partitioning only occurs when the overriding plate contains a weakness, either in the form of thinned or faulted lithosphere. Thus, the inherited weakness seems to be a key factor exerting control on sliver tectonics (Chemenda et al. 2000; Haq and Davies, 2010; Cooke et al. 2020). Strain partitioning and consequent sliver motion have been assessed from multiple approaches (i.e., numerical and analog models, and observations in nature). However, the role of slab dynamics in sliver tectonics is still poorly understood.

To better understand the conditions leading - or not - to strain partitioning and sliver motion during the different stages of subduction evolution, we perform a set of 3-D upper mantle-scale subduction experiments (Fig. 1). In particular, we systematically test the effect of the convergence obliquity on subduction dynamics and strain location in the overriding plate. We also simulate the presence of an inherited structure at the arc-forearc interface through the inclusion of a lithospheric scale weak zone in the models to understand the role of inheritance on sliver tectonics. With some cautions, the modeling results could finally be used to shed light on the orogenic evolution along active margins with sliver tectonics.

2. METHODOLOGY

In this section, we describe the experimental setup and materials used to reproduce oblique subduction in our analog laboratory experiments (Fig. 1). The experimental parameters of each model are detailed in Table 1.

2.1. Experimental setup and procedure. The experimental set-up adopted in our experiments has been largely tested by several authors (e.g., Funiciello et al. 2003; Martinod et al. 2005), yielding interesting insights on the link between subduction zone dynamics and overriding plate strain (e.g., Heuret et al. 2007; Espurt et al. 2008; Guillaume et al. 2009, 2018; Martinod et al. 2013; Chen et al. 2016). The experimental set-up simulates a lithosphere and sub-lithospheric upper mantle system, with plates made of different silicones and the sub-lithospheric mantle simulated by glucose syrup (Fig. 1). This is a simplified version of subduction systems in nature, hence it presents limitations as detailed by Funiciello et al. (2003) and Martinod et al. (2013), for instance. One of the main restrictions of this experimental setup is the lack of thermal effects that cannot be accounted for in the laboratory.

Materials used to model the subduction system are placed inside a 100 x 100 x 30 cm Plexiglas tank (Fig. 1). The bottom of the tank is rigid, simulating an upper-lower mantle impermeable discontinuity at 660-km depth (Fig. 1; Funiciello et al. 2003). This is an approximation of the natural system, in which the upper-lower mantle discontinuity rather corresponds to a jump in viscosity of one to two orders of magnitude (e.g., Steinberger and Calderwood, 2006; Nakada et al., 2018). However, tomographic images of current subduction zones around the world show fast velocity anomalies (interpreted as stagnant slabs) lying almost flat at the upper-lower mantle transition zone in some places (e.g., Western Pacific; Li et al. 2008) and slab unfolding models of present and past subduction zones also show that the 660 km discontinuity corresponds to the top of a slow-down zone for the slab sinking velocity (van der Meer et al. 2018). Both observations suggest that over periods of a few 10's My, the upper-lower mantle discontinuity may act as a relatively impermeable

boundary. Therefore, we limit the experiment duration to less than 30 min (scaling to 60 My, see below).

The sub-lithospheric mantle is simulated by a 10-cm thick layer of low-viscosity glucose syrup (Fig. 3), corresponding to ~660-km thick in nature, which yields a length scale factor $L^* = L_{model} / L_{nature}$ of 1.5×10^{-7}. The viscosity of this layer is independent of shear rate (Schellart, 2011) and varies between 60 and 81 Pa.s depending on the temperature in the laboratory (Salze et al. 2018). On top of the layer of glucose syrup, we deposit the subducting (oceanic) and overriding (continental) plates (Fig. 1) made of PDMS silicone (Polydimethylsiloxane Silicone) mixed with iron powder to achieve the required densities. We use a higher density for the subducting plate (ρ_{mantle} - ρ_{plate} = [-52;-38] kg/m^3) to allow spontaneous gravity-driven subduction, while the continental lithosphere was simulated by a lower density compound (ρ_{mantle} - ρ_{plate} = [126;148] kg/m^3) (Table 1). The viscosity of the oceanic silicone is ~10^5 Pa.s giving a slab to mantle viscosity ratio in the range 1235-1666, and the viscosity of the overriding plate is ~8.5×10^4 Pa.s. In the overriding plate, we simulate in all models the presence of a weak volcanic arc by using a 2-cm large (equivalent to 132 km in nature) strip of pure PDMS, with a smaller viscosity of 3.5×10^4 Pa.s (Fig. 1), located at a distance of 3 cm (equivalent to ~200 km in nature) away from the trench. In all experiments, the subducting and overriding plates are decoupled by a thin (~1mm) layer of petrolatum (20-30%) mixed with paraffin oil (70-80%) to simulate a weak subduction interface (following the procedure of Duarte et al. 2013, 2014), which also prevents plates sticking effects. In the experiments with an inherited discontinuity between the forearc and arc, both areas are initially decoupled by a vertical cut lubricated with the same mixture used at the subduction interface. The lateral distance between the plates and the sides of the Plexiglas tank

is at least 26.5 cm, which is larger than the size of convective cells within the upper mantle (~10 cm) to minimize lateral boundary effects (Funiciello et al. 2004).. The width of the subducting plate (W_s) is changed between experiments according to the obliquity angle to keep a constant trench width of ~40 cm (Fig. 1). Indeed, previous studies have shown that the width of the subduction zone can exert a first-order control on trench and subduction velocity (e.g., Schellart et al. 2007; Guillaume et al. 2010), possibly modifying upper plate deformation. The obliquity angle (Φ) is defined as the angle between the trench and convergence directions, meaning that Φ = 90° corresponds to trench-orthogonal convergence and a decreasing Φ value to an increasing obliquity. We test values of 80°, 60°, and 30° for Φ (Fig. 1).

Subduction is initiated by manually pushing the leading edge of the subducting plate into the glucose syrup down to a depth of 2-3 cm. The convergence during subduction is driven by both the gravity effect owing to the negative buoyancy of the subducting lithosphere (i.e., slab pull) and by an additional push at a constant velocity of 1.5 cm/min at the trailing edge of the subducting plate (Fig. 1). This convergence rate scales to ~5 cm/yr in nature (see below), which is close to the mean trench-orthogonal converce rate measure at present-day subduction zones of 4.7±2.9 cm/yr (Lallemand and Heuret, 2017). In all models, the overriding plate is fixed, imposing a no-velocity condition for the upper plate. The duration of experiments varies between 23 and 29 min.

Following the procedure described in Guillaume et al. (2021), and considering a viscosity for the sub-lithospheric mantle of $5x10^{20}$ Pa.s, we obtain the following scaling between the lab and nature: 1 minute in the lab corresponds to ~2 Myr in nature (scalling factor $t^* = t_{model} / t_{nature} = 9.5 \times 10^{-13}$) and a velocity of 1 cm/min to

~3.2 cm/yr in nature (scaling factor $U^* = U_{model} / U_{nature} = 1.64 \times 10^5$), meaning that the imposed subducting plate motion corresponds to ~5 cm/yr.

2.2. Tracking displacement and strain in the experiments. The evolution of the models is monitored by cameras located at the top and on one side of the experiments taking pictures every 30 seconds. On the lateral views, we measure the dip of the slab at the lateral boundary of the subduction zone at a depth of ~3 cm (~200 km in nature). On the top views, we measure the convergence-parallel longitudinal strain (or elongation) across the center of the overriding plate. We also use the PIV (Particle Image Velocimetry) technique with the *PIVlab* software (Thielicke, 2014; Thielicke and Stamhuis, 2014) to obtain a regular velocity field that is further used to calculate the mean displacement vector of the sliver forearc. In addition, we drew a regular grid of white points at the surface of the plates to automatically track the trajectories of material points during the model evolution. For this, we use the PTV (Particle Tracking Velocimetry) technique, implemented in the *TracTrac* software (Heyman, 2019). We then use the velocity at single points to compute the strain components with the *SSPX* software (see Cardozo and Allmendinger, 2009, for details). By using a minimum of three points (or stations) in 2D, this software calculates the best-fitting strain tensors (i.e., displacement gradient tensor, g_{ij}) from previously obtained velocity vector data. The tensor is split up into symmetric (ε_{ij}) and antisymmetric (ω_{ij}) tensors. The symmetric tensor allows the calculation of the principal quadratic elongations, i.e., λ_{max} and λ_{min}, as classically defined as the square of the stretch (S) (Ramsay and Huber, 1983). It also calculates the orientation (θ) and magnitude (γ_{max}) of the maximum shear strain, defined as the tangent of the angular change between two lines that are assumed to be initially

orthogonal. We compute strain from pairs of pictures taken one minute apart using a nearest-neighbor approach.

3. EXPERIMENTAL RESULTS

A set of upper mantle-scale laboratory experiments was performed to simulate oceanic lithosphere subduction at variables convergence angles, from trench-normal (Φ= 90°) to highly trench-oblique convergence (Φ= 50°), beneath a continental lithosphere (Fig. 1). In order to gain insights into the kinematics of continental slivers, we tested two end-members: one without a weak zone between the arc and forearc in the overriding continental lithosphere (models 1 to 4), and one with a weak zone between the arc and forearc (models 5 to 7), obtained by pre-cutting the lithosphere and filling it with a low-viscosity mixture (paraffine oil + petrolatum), roughly mimicking an inherited lithospheric-scale discontinuity or plate softening by the magmatic arc. The parameters of the seven models are listed in Table 1.

Materials and parameters		**Units**	**Ref. Exp.**	**Trench-oblique convergence**					
			Model-01	*Model-02*	*Model-03*	*Model-04*	*Model-05*	*Model-06*	*Model-07*
Subducting plate	Length "L_{1SP}"	cm	50	50	52	55.5	42	48	49
	Width "W_{SP}"	cm	40	38.3	34.2	30	37.4	33	30.5
	Thickness "Th"	cm	1.2	1.2	1.2	1.2	1.2	1.2	1.2

	Density "δ_{SP}"	Kg/m3	1470	1470	1470	1483	1470	1484	1484
	Buoyancy (δ_{SP} - δ_{um})	Kg/m3	-38	-38	-38	-51	-38	-52	-52
Overriding plate	Length "L_{1OP}"	cm	31	32	42	45	49	44	43
	Width "W_{OP}"	cm	47	43	44	45	36	41	39
	Thickness "Th"	cm	0.77	0.77	0.77	0.77	0.77	0.77	0.77
	Density "δ_{OP}"	Kg/m^3	1284	1284	1284	1306	1284	1292	1292
	Buoyancy (δ_{OP} - δ_{um})	Kg/m^3	148	148	148	126	148	140	140
Trench	Width (W_T)	cm	40	40	40	39.5	40	40	40
Obliquity	Angle (Φ)	°	90	80	60	50	80	60	50
Forearc Discontinuity	Yes/No		No	No	No	No	Yes	Yes	Yes
Upper mantle	Thickness "Th"	cm	9.6	9.6	9.6	10	9.6	9.6	9.6
	Density "δ_{um}"	Kg/m^3	1432	1432	1432	1432	1432	1432	1432
	Viscosity	Pa s	60,4	60,4	71,4	73,5	75,7	81,2	74,6

Table 1. Experimental parameters. For reference of the parameters and their geometrical meaning, see figure 3.

3.1. Reference model (MODEL-01): subduction with trench-orthogonal convergence (Φ = 90°). The reference model of subduction presented in this section (Model-01) simulates trench-orthogonal convergence.

3.1.1. Subduction dynamics. During subduction initiation, before the slab interacts with the bottom of the box simulating the lower mantle, the slab sinks with increasing subduction velocity. It is accompanied by a progressive steepening of the slab reaching dip values up to 40-42° (Fig. 2). During this first phase, the trench retreats toward the subducting plate at rates of 0.43 cm/min driving trench-orthogonal stretching of the overriding plate (Fig. 2). After 6 min, the leading edge of the slab reaches the bottom of the tank (Fig. 2). The arrival of the slab at the bottom of the tank produces slab forward folding, and as a consequence, the slab dip progressively decreases to values as low as ~20° (Fig. 2). This stage of slab shallowing is accompanied by trench advance toward the overriding plate and trench-orthogonal horizontal shortening across the overriding plate, whose absolute velocity is fixed to zero (Fig. 2). The shift from stretching to shortening is marked by a short adjustment stage (~4 min) of neutral overriding plate deformation. After 20-21 min of subduction driven by slab pull and imposed subducting plate trenchward displacement, the length of the slab fold becomes too long and gravitationally unstable, leading to a decrease of its radius of curvature at the trench, i.e. the shallow part of the slab becomes progressively steeper (Fig. 2).

3.1.2. Overriding plate deformation. The convergence parallel longitudinal strain (here corresponding to the along-x component of deformation) of the overriding plate keeps a straightforward relationship with trench motion, as well as with the slab geometry (Fig. 2). Trench retreat favors horizontal stretching or neutral conditions. Instead, trench advance triggers shortening (Fig. 2), whose intensity is modulated by

the slab geometry (a larger amount of shortening during slab shallowing and a smaller amount of shortening during slab steepening). There are no clear patterns of shear strain in this reference experiment (Fig. 3). Despite the overriding plate embedding a weaker arc, the amount of deformation does not appear to have a strong localization in this area but is rather homogeneously distributed at plate scale (Fig. 4).

Additionally, by tracking the path of individual particles during experiment evolution, we can describe the flow parameters for further characterization of the strain state and degree of coaxiality in the entire overriding plate. In our models, the kinematic vorticity number (W_k; see Fossen and Tikoff, 1993, and Fossen, 2010) appears to be a useful measure (assuming cases of steady-state flow) to evaluate how close overriding plate deformation is from simple shear or pure shear, being $W_k = 1$ for pure shear, $W_k = 0$ for simple shear, and W_k is between 0 and 1 for sub-simple shear. W_k is defined, as follows:

$$Wk = cos\,\alpha$$

where α is the intersection angle between flow apophyses. For cases where α ≠ 90°, the calculation is made from the acute angle.

In the reference experiment, at the plate-scale, the 2D strain state in the overriding plate is pure shear-dominated, i.e., $W_k = 0$ (Fig. 5).

3.2. Subduction models with trench-oblique convergence. In these experiments, we systematically decreased the angle between the trench and the convergence direction from Φ=80° (Model-02 and Model-05), to Φ=60° (Model-03 and Model-06), and Φ=50° (Model-04 and Model-07), thus increasing obliquity (Fig. 1B and Table 1).

For each convergence angle, we simulate two end-members with the forearc either fully coupled or decoupled from the rest of the plate.

3.2.1. Slab geometry. Slab geometry first-order evolution is similar to that of the reference experiment for all models, i.e., alternating periods of slab steepening and slab shallowing. The trench-oblique subduction experiments exhibit an initial phase of slab sinking and steep slab dip, then the slab reaches the bottom of the tank. Depending on the way subduction is initiated we observe a delay for the arrival of the slab at the 660-km discontinuity between the two sides of the subduction zone that is generally around 1-2 minutes, except for Model-04 where it is 6 minutes. After both sides of the slab reached the bottom of the tank, the slab folds forward, producing a decrease of the slab dip close to the surface. The slab fold then becomes unstable and collapses, and a new stage of slab steepening close to the surface starts.

3.2.2. ***Overriding plate deformation.*** Like in the reference model, the convergence-parallel longitudinal strain of the overriding plate adjusts to trench kinematics and slab geometry. A steep slab dip favors a neutral-to-stretching regime across the overriding plate, while slab shallowing induces overriding plate shortening (Fig. 6). However, at the plate scale, the two-dimensional strain state departs from pure shear to enter the sub-simple shear field, meaning that large-scale deformation becomes non-coaxial (Fig. 5). By tracking individual particle paths, one can identify flow apophyses associated with upper plate deformation. The kinematic vorticity number (W_k) increases with increasing obliquity (Fig. 5).

Strain is preferentially accommodated within the forearc and arc regions (Figs. 3 and 4) in absence of a pre-existing fault. However, the distribution of strain varies over space and time (Figs. 3 and 4). During the first stage of slab sinking in Model-03, the

maximum shear strain rate is low across the overriding plate (< 10^{-2} min^{-1}) (Fig. 3). Then, when both sides of the slab reach the bottom of the tank, and convergence-parallel shortening is ongoing, higher rates of shear strain of around 1-2x10^{-2} min^{-1} are recorded in the forearc.

For the equivalent models with an inherited discontinuity at the arc-forearc interface, the deformation pattern is strongly modified. In these models, strong variations of the strain components are observed across the overriding plate (Figs. 3 and 4). In Model-06, the arc absorbs the largest rates of shear strain reaching values larger than 5x10^{-2} min^{-1}. Values of 10^{-2} min^{-1} are observed in the forearc, while the retroarc shows lower rates of shear strain (< 10^{-2} min^{-1}) (Figs. 3 and 4). At the end of the experiment, the forearc is underthrusted, and the retroarc records larger amounts of strain (Fig. 3; see also **Supplementary Material 1**).

3.2.3. ***Sliver motion.*** In the experiments that do not include a discontinuity at the forearc-arc interface, there is no independent motion of the forearc with respect to the rest of the overriding plate, i.e. no sliver tectonics. Instead, in the models that include a discontinuity at the arc-forearc interface, the forearc block follows a three-step kinematic history. During the first stage, the slab sinks at a high angle (Fig. 7), and the trench retreats toward the oceanic plate. The forearc follows the motion of the retreating trench. Since the oceanward motion of the forearc is faster than the motion of the rest of the overriding plate, a gap or channel opens at the arc-forearc interface (Fig. 7) that is filled with low-viscosity glucose syrup (equivalent to the sub-lithospheric mantle in nature) and the forearc behaves as an independent block from the rest of the overriding plate, i.e., as a sliver block. The second stage starts when the longest side of the slab reaches the bottom of the tank (Fig. 8). It is associated with trench advance, triggering the motion of the forearc sliver block toward the

continent (Figs. 7 and 8). The transition from stage 1 to stage 2 is marked in the forearc by lower ratios between the trench-parallel and trench-orthogonal components of velocities (V_p / V_o) (Fig. 8). The advance of the forearc results in the closing of the channel opened between the forearc and arc and finally leads to the forearc accretion against the rest of the overriding plate and the closing of the channel opened between the forearc and arc (Fig. 7). During this stage, the V_p / V_o ratio increases (Fig. 8).

The total displacement of the sliver forearc with respect to the arc over periods of 23-24 min (equivalent to ~46-48 Myr, or 2325±50 km of convergence in nature) varies among the models: it is between 0.9±0.1 (59±7 km in nature) for the case of low obliquity (Φ = 80°), between 6.1±0.8 cm (403±53 km in nature) for the case of moderate obliquity (Φ = 60°), and 8.6±0.2 cm (566±14 km in nature) for the case of high obliquity (Φ = 50°) (Fig. 9). It translates into mean strike-slip rates that vary between 0.03 cm/min and 0.39 cm/min (0.1 cm/yr to 1 cm/yr in nature), which represents only a fraction of the trench-parallel component of convergence velocity (0.26 cm/min for Φ = 80° to 0.96 cm/min for Φ = 50°). It should be noted that the displacement is not constant over time and that the highest values of forearc trench-parallel velocity are observed during the first phase of subduction and immediately after the slab touches the bottom of the tank. In the model with the highest obliquity, for instance, the trench-parallel sliver velocity is close to the trench-parallel component of convergence, i.e. ~1 cm/min (3.2 cm/yr in nature) (Fig. 9). Interestingly, periods of slower trench-parallel displacements of the sliver forearc correlate with periods of faster trench-orthogonal relative motion between the forearc and backarc, i.e., faster shortening in this area (Fig. 9).

4. INTERPRETATION AND DISCUSSION

4.1. Subduction dynamics and overriding plate deformation. Subduction models have been performed to give insights into the interplays of forces acting on the subduction system and their control on the slab geometry, plate and trench motions and *in fine* the strain regime within the overriding plate (e.g., Funiciello et al. 2003, 2004; Bellahsen et al. 2005; Martinod et al. 2005, 2013; Schellart, 2005; Heuret et al. 2007; Espurt et al. 2008; Guillaume et al. 2009; Chen et al. 2016). Previous experiments have shown a straightforward relationship between the slab dip, the trench motion, and the strain regime of the overriding plate (e.g., Heuret et al. 2007; Guillaume et al. 2009). In these models, steep slab dip and trench retreat associated with slab roll-back induce a trench-orthogonal stretching of the overriding plate, while trench-orthogonal shortening is triggered by shallow slab dip and advancing trench (e.g., Guillaume et al. 2009). Slab dip variations measured at depths equivalent to ~200-300 km in nature are controlled by the episodic slab folding, resulting from interaction of the slab with the upper-lower mantle transition and the applied horizontal boundary conditions (see further details in Guillaume et al. 2009). While an impermeable upper-lower mantle transition favors slab folding, alternations of periods of slab shallowing and steepening are also obtained in numerical models employing a stratified mantle with a viscosity jump at the upper-lower mantle discontinuity of one to two orders of magnitude (e.g., Garel et al., 2014; Briaud et al. 2020), even for slabs penetrating the lower mantle.

We observe similar behavior in our reference model with trench-orthogonal convergence (Model-01). In models with oblique convergence, the convergence-parallel longitudinal strain also shows episodes of stretching during the initial stage of subduction and trench retreat and successive shortening phases associated with

slab forward folding and trench advance (Fig. 6). The convergence angle does not modify the subduction dynamics and the overall pattern of convergence-parallel longitudinal state of strain, implying that it is mainly controlled here by the boundary conditions, i.e., a fixed overriding plate and a constantly advancing subducting plate. However, the two-dimensional horizontal state of strain appears strongly modified by the convergence angle. At the plate scale, a decrease of the trench-oblique convergence angle (Φ), i.e., a shift from trench-orthogonal convergence toward trench-parallel convergence, induces a shift from pure shear toward increasing sub-simple shear (Fig. 5). These results are in agreement with those from numerical models quantifying strain under transpressional states (e.g., Fossen and Tikoff, 1993; Fossen et al. 2004). However, in orogenic systems, the strain can be across-strike heterogeneously distributed, including in the internal domains (Fossen and Tikoff, 1993, 1998). Our laboratory experiments for the cases of trench-oblique convergence indeed show that magnitude and components of strain are partitioned between the forearc, the weaker arc, and the retroarc lithospheric domains (Fig. 3). Cooke et al. (2020) using crustal-scale models, also showed that under low-to-moderate angles of convergence the slip is efficiently distributed over strike-slip and thrust faults. Modeling results appear consistent with many geological models of strain partitioning proposed, for example, for the Andean orogen (e.g., Cembrano et al. 2002; Folguera and Ramos, 2002), where the volcanic arc undergoes transpression with high rates of denudation (Thomson, 2002) concomitant with the ongoing growth of retroarc fold-and-thrust belt (Cembrano et al. 2002; Folguera and Ramos, 2002; Echaurren et al. 2022).

4.2. Sliver tectonics and the role of inherited structures. In subduction zones characterized by trench-oblique convergence, portions of the forearc can undergo

coastwise-parallel transport (*sensu* Beck, 1991). These pieces of forearc, known as sliver plates or blocks, are decoupled from the rest of the overriding plate and offset along trench-parallel faults (Fitch, 1972; Jarrard, 1986b; Beck, 1991; Beck et al. 1993; Nelson et al. 1994; Fossen and Tikoff, 1998; Haq and Davies, 2010). Some authors (e.g., Beck, 1991; Chemenda et al. 2000) argued that the sliver motion is favored by high trench-oblique convergence, a shallow slab dip, high-coupling in the subduction interface (i.e., interplate friction), and the presence of a weakness in the overriding plate.

Chemenda et al. (2000) using laboratory experiments demonstrated that sliver motion (evidence of slip partitioning) only occurred if the overriding plate embeds a weakness, being either a thinned or a faulted crust. Our experimental results are consistent with this observation since the decoupling and trench-parallel motion of the forearc sliver is only possible in the subduction experiments embedding a discontinuity/weakness within the overriding plate, here simulating a discrete, inherited fault along the forearc-arc interface at the lithospheric scale. In this way, the discontinuity allows strain localization and the independent motion of the forearc sliver from the rest of the overriding plate.

Additionally, Chemenda et al. (2000) argued that the sliver motion is effective under conditions of high interplate friction. The friction force (F_f) is defined (see Chemenda et al. 2000), as follows:

$$F_f = S\tau_n$$

where S is the interplate surface and τ_n the interplate friction stress. It can be decomposed into vertical (F_{fz}), along-trench (F_{fy}), and trench-orthogonal (F_{fx}) components, as follows:

$$F_{fz} = F_f \cos\Phi' \sin\beta;\ F_{fy} = F_f \sin\Phi';\ F_{fx} = F_f \cos\Phi' \cos\beta;$$

with β the slab dip angle measured close to the surface, and Φ' the obliquity angle, which equals 90°- Φ (see figure 1 for geometrical meaning). The along-trench translation of the forearc sliver results from the along-trench component of the friction force (F_{fy}). A larger obliquity angle (Φ') promotes strain partitioning and sliver lateral motion (Chemenda et al. 2000). Our subduction experiments confirm that, there is indeed an increase of the trench-parallel displacements as Φ decreases from 80° to 50°, i.e. increasing convergence obliquity (Fig. 9).

An additional consequence of the underlying physics to the above-stated equations is the effect of slab geometry on strain partitioning. Under low angles of subduction (β), the interplate surface increases, increasing the friction force (F_f) for constant interplate friction stress (τ_n). It implies that the along-trench component of the friction force should increase and the sliver motion should be favored. However, our subduction experiments do not show such a clear picture. Indeed, during stage 2, following slab anchoring in the lower mantle, the slab dip is generally shallower than during stage 1. If this decrease in slab dip indeed corresponds to an increase in the trench-parallel motion of the sliver block in Model-07, with the highest obliquity (Fig. 8), it is not the case for Model-05 and Model-06 where a decrease in V_p is rather

observed. It therefore suggests that other processes can become dominant and prevent the sliver block from moving parallel to the trench.

Interestingly, we have shown that the subduction involves periods of detachment and accretion of the sliver block, and not only trench-parallel slip, as classically treated. In fact, the highest amount of lateral transport is achieved during the stage of detachment and oceanward motion, independently of the slab geometry. This can be understood by considering the shear force (F_a) exerted on the vertical low-viscosity channel corresponding to the forearc-arc discontinuity:

$$F_a \sim \eta_m \times V_p \times \frac{L}{W} \times H$$

with η_m the viscosity of the channel, Vp the forearc sliver trench-parallel velocity, L, H and W the length, height, and width of this channel, respectively. For a constant F_a, which approximates here F_{fy}, and a constant length of the sheared channel, an increase in the width of the channel requires an increase in Vp, therefore a faster sliver trench-parallel motion. In turn, a decrease of the width of the channel should be followed by a decrease of the trench-parallel sliver velocity. In Model-07, the channel closure starting after 2 minutes does not correlate instantaneously with a decrease of the sliver block trench-parallel velocity. The competing effect of slab dip decrease at the same time prevents the slow down, which only occurs once the channel is closed and W has become very small and H has increased, i.e. after ~14 min (Fig. 9)

Plate convergence obliquity, slab dip, and overriding plate heterogeneities appear as the main factors exerting control on sliver tectonics. The formation of a sliver block would therefore be promoted by an inherited fault running parallel to the trench direction and, as expected, by a high-angle of trench-oblique convergence. However,

even for near trench-orthogonal convergence (Φ = 80°), shear strain localizes along the forearc-arc discontinuity and dextral offset is observed. Instead, in the absence of inherited structures, even the largest obliquity (Φ = 50°) does not result in a significant offset between the forearc and arc. In this case, shear strain is preferentially accommodated within the weak arc but there is no individualization of an independent forearc sliver.

4.3. Evolution of subduction-related orogens with sliver blocks. Most of the laboratory experiments designed to gain insights into the forces acting on the sliver motion, and their further kinematic implications, have focused on crustal-scale experiments using clay or sand (e.g., Haq and Davis, 2010, Leever et al. 2011, Cooke et al. 2020; among others). For example, Haq and Davis (2010) developed analytical solutions and analog models to evaluate the ratio between the strike-slip rate and the total convergence rate as a function of both the obliquity of plate convergence and varying rheologies. They found that models with or without a defined sliver plate are very difficult to distinguish based on the topography of the wedge for the same obliquity but can be assessed by characterizing the 2-D strain field and style of deformation. Cooke et al. (2020) using crustal-scale clay experiments also showed that strain partitioning occurs under a wide range of experimental conditions, and it could be classified into three categories that are controlled by both the angle of convergence and pre-existing weaknesses. Both studies show that pre-existing weak zones foster slip partitioning, which is in agreement with the first-order observation of our models. However, further comparison of strain pattern and strain evolution is not possible because of the different rheologies (viscous vs, brittle/frictional) and scales (mantle vs. crustal) used.

Our models, despite their inherent limitations (e.g., no trench-parallel strength variations within the upper plate, a fixed upper plate, a continuous subducting slab, and a 660-km discontinuity that remains impermeable for periods < 60 Myr) allow completing these previous studies by incorporating slab dynamics into the system and looking at the long-term (>10 Ma) evolution of active margins. In our models, the free sinking of the slab during the first stage is accompanied by slab roll-back that favors an extensional tectonic regime within the overriding plate, whatever the obliquity of the convergence. The presence of an inherited discontinuity along the forearc-arc interface, as simulated in the case of models with low forearc-arc coupling, strongly controls the deformation location (Fig. 4). In this set of experiments, the slab roll-back and trench retreat drag the forearc toward the oceanic plate, decoupling the forearc sliver from the rest of the overriding plate. The forearc sliver motion results in the opening of a gap or channel along the forearc-arc interface (Fig. 7), which is filled by the upwelling of glucose syrup, our analog for the asthenospheric mantle in nature. Therefore, the subduction experiments suggest that oceanward translation and detachment of sliver blocks could be an effective mechanism to explain orogenic systems with a hyperextended forearc accompanied by the exhumation of upper mantle rocks (Fig. 10; e.g., Hervé et al. 1995, 2017; Maffione et al. 2015).

Once the slab is anchored at the 660-km discontinuity, the overriding plate shifts to an overall strain regime characterized by convergence-parallel shortening associated with slab shallowing and trench advance. In the subduction experiments with an inherited discontinuity at forearc-arc transition, the shortening across the overriding plate is accompanied by the landward motion of the forearc sliver and its accretion against the rest of the overriding plate (figs. 7 and 10). During the accretion of the

forearc sliver, decreases the trench-parallel motion, and the shear strain is broadly focused along the arc domain (Fig. 4). The dextral lateral motion occurs at rates equivalent to 0.7 cm/yr and 0.9 cm/yr for Model-06 and Model-07, respectively. In both cases, it corresponds to ~30% of the trench-parallel component of the imposed convergence, highlighting the difficulty of distinguishing the obliquity of convergence based on the amount of lateral displacement, as previously stated by Haq and Davis (2010). The accretion process accompanying trench advance ultimately results in the underthrusting of the forearc under the arc, and contraction across the entire upper plate (Fig. 5), which in natural systems could be observed as a doubly-vergent orogenic architecture. Such doubly-vergent orogens associated with subduction have been described along the South American margin, for instance, at places where strike-slip faulting is active like in northern Patagonia (e.g., Echaurren et al. 2022) and where no strike-slip fault is active like in the Central Andes (e.g., Armijo et al. 2015).

Our modeling study also confirms that a distinction between plate margins with or without sliver requires a precise strain analysis, which may turn out to be difficult, especially for cases of ancient orogens where many orogenic pieces could have been eroded.

5. CONCLUSIONS

We perform analog models to understand the influence of oblique convergence on the subduction dynamics and overriding plate deformation. The 3-D subduction experiments show that whatever the obliquity of convergence, slab evolution alternates between steepening and shallowing periods, associated with stages of convergence-parallel stretching (or moderate shortening) and stages of significant

shortening of the overriding plate, respectively. We also show that in models without a pre-existing forearc-arc discontinuity, when increasing convergence obliquity, the 2-D strain state of the overriding plate departs from pure shear and enters into the field of the sub-simple shear, but without individualizing a sliver forearc block. Indeed, sliver tectonics is only achieved if the overriding plate embeds an inherited weakness, here localized along the forearc-arc interface, and the amount of lateral offset, as well as the mean offset velocity increases when departing from trench-orthogonal convergence.

We also show that variations of slab geometry and forearc-arc discontinuity geometry during subduction modulate the trench-parallel motion of the forearc sliver. In particular, we show that slab shallowing increases the stresses that apply on the intraplate fault separating the forearc sliver from the rest of the continental plate, leading to a slower sliver displacement.

Finally, our experimental results could be applied to some extent to natural subduction-related orogenic systems. Hyperextension of the forearc accompanied by the exhumation of upper mantle rocks and significant lateral offset of the sliver block could be a result of trench retreat and reduced interplate coupling during the initial stage of slab sinking. Slab anchoring within the lower mantle may induce the sliver block accretion and lateral displacement to slow down, which could ultimately result in arc underthrusting and shortening across the entire plate, potentially shaping doubly-vergence orogen architecture.

6. ACKNOWLEDGMENTS

This research is part of a bilateral scientific cooperation project between Argentinian Mincyt –Universidad de Buenos Aires, and the Besançon University (France), funded

by the Argentinian-French ECOS-SUD under grant project A15U02 (C.S. and M.G.). Financial support was also provided by projects CONICET PIP 11220200100307CO, UBACYT GC 20020190100382BA, and PICT-2020-SERIEA-03277 awarded to MG. RS is thankful to Cécile Bougma for helping in experiment preparation and Carlos Fernández for assistance during stay in the laboratory at University of Rennes 1. Fruitful discussions with Andrés Echaurren, Paulo Quezada, and the LAMOGE staff (Laboratorio de Modelado Geológico, UBA-CONICET) enriched this work. We would also like to thank the Editor Samuel Angiboust, as well as Onno Oncken and two anonymous reviewers, for their constructive comments that contributed improving the final version of this article.

7. SUPPLEMENTARY MATERIAL 1. Maximum shear strain at different times for the Model-02, Model-04, Model-05, and Model-07.

8. DATA AVAILABILITY

See the dataset supporting this article on the following link: https://dataservices.gfz-potsdam.de/panmetaworks/review/7355c7fd6018b2e54e78a284f3adb9e7b65948324f7b1bcc539c5393c3c2efa8/

9. REFERENCES

1. Armijo, R., Lacassin, R., Coudurier-Curveur, A., Carrizo, D., 2015. Coupled tectonic evolution of Andean orogeny and global climate. Earth-Science Reviews, 143, 1-35. https://doi.org/10.1016/j.earscirev.2015.01.005.

2. Balázs, A., Faccenna, C., Ueda, K., Funiciello, F., Boutoux, A., Blanc, E. J.-P., Gerya, T., 2021. Oblique subduction and mantle flow control on upper plate deformation: 3D geodynamic modeling. Earth and Planetary Science Letters, 569, 117056. doi:10.1016/j.epsl.2021.117056.

3. Beck Jr, M.E., 1983. On the mechanism of tectonic transport in zones of oblique subduction. Tectonophysics, 93, 1-11.

4. Beck Jr, M.E., 1991. Coastwise transport reconsidered: lateral displacements in oblique subduction zones, and tectonic consequences. Physics of the Earth and Planetary Interiors, 68, 1-8.

5. Beck Jr, M.E., Rojas, C., Cembrano, J. 1993. On the nature of buttressing in margin-parallel strike-slip fault systems. Geology, 21, 755-758.

6. Bellahsen, N., Faccena, C., Funicciello, F., 2005. Dynamics of subduction and plate motion in laboratory experiments: Insights into the ‘‘plate tectonics’’ behavior of the Earth. Journal of Geophysical Research, 110, B01401.

7. Briaud, A., Agrusta, R., Faccenna, C., Funiciello, F., van Hunen, J., 2020. Topographic Fingerprint of Deep Mantle Subduction. Journal of Geophysical Research: Solid Earth, 125, e2019JB017962. https://doi.org/10.1029/2019JB017962

8. Cardozo, N., Allmendinger, R.W., 2009. SSPX: A program to compute strain from displacement/velocity data. Computers & Geosciences, 35, 1343–1357.

9. Cembrano, J., Lavenu, A., Reynolds, P., Arancibia, G., López, G., Sanhueza, A., 2002. Late Cenozoic transpressional ductile deformation north of the Nazca–South America–Antarctica triple junction. Tectonophysics, 354, 289–314.

10. Chemenda, A., Lallemand, S., Bokun, S., 2000. Strain partitioning and interplate friction in oblique subduction zones: Constraints provided by experimental modelling. Journal of Geophysical Research, 105, B3, 5567-5581.

11. Chen, Z., Schellart, W.P., Strak, V., Duarte, J.C., 2016. Does subduction-induced mantle flow drive backarc extension? Earth and Planetary Science Letters, 441, 200-210.

12. Cooke, M.L., Toeneboehn, K., Hatch, J.L., 2020. Onset of slip partitioning under oblique convergence within scaled physical experiments: Geosphere, 16, 3, 875–889. https://doi.org /10.1130/GES02179.1.

13. Duarte, J.C., Schellart, W.P., Cruden, A.R., 2013. Three-dimensional dynamic laboratory models of subduction with an overriding plate and variable interplate rheology. Geophysical Journal International, 195, 1, 47-66. doi:10.1093/gji/ggt257.

14. Duarte, J.C., Schellart, W.P., Cruden, A.R., 2014. Rheology of petrolatum-paraffin oil mixtures: Applications to analogue modelling of geological processes. Journal of Structural Geology, 63, 1-11.

15. Echaurren, A., Encinas, A., Sagripanti, L., Gianni, G; Zambrano, P., Duhart, P., Folguera, A., 2022. Fore-to-retroarc crustal structure of the north Patagonian margin: How is shortening distributed in Andean-type orogens? Global and Planetary Change, 103734. https://doi.org/10.1016/j.gloplacha.2022.103734

16. Espurt, N., Funiciello, F., Martinod, J., Guillaume, B., Regard, V., Faccenna, C., Brusset, S., 2008. Flat subduction dynamics and deformation of the South American plate: insights from analog modeling. Tectonics, 27.

17. Fitch, T.J., 1972. Plate convergence, transcurrent faults, and internal deformation adjacent to Southeast Asia and the western Pacific. Journal of Geophysical Research 77: 4432–4460.

18. Folguera, A., Ramos, V., 2002. Partición de la deformación durante el Neógeno en los Andes Patagónicos Septentrionales (37° 46° S). Rev. Soc. Geol. España, 15, 1-2, 81-93.

19. Fossen, H., Tikoff, B., 1993. The deformation matrix for simultaneous simple shearing, pure shearing and volume change, and its application to transpression-transtension tectonics. Journal of Structural Geology, 15, 3-5, 413-422.

20. Fossen, H., Tikoff, B. 1998. Extended models of transpression and transtension, and application to tectonic settings. In: Holdsworth, R.E., Strachan, R.A., Dewey, J.E. (eds), Continental Transpressional and Transtensional Tectonics. Geological Society, London, Special Publications, 135, 15-33.

21. Fossen, H., Tikoff, B., Teyssier, C., 2004. Strain modelling of transpressional and transtensional deformation. Norsk Geologisk Tidsskrift, 74, 134-145.

22. Fossen, H., 2010. Structural Geology. Cambridge University Press, 463p. Cambridge.

23. Funiciello, F., Faccena, C., Giardini, D., Regenauer-Lieb, K., 2003. Dynamics of retreating slabs: Insights from three-dimensional laboratory experiments. Journal of Geophysical Research, 108, B4.

24. Funiciello, F., Faccenna, C., Giardini, D., 2004. Role of lateral mantle flow in the evolution of subduction systems: insights from laboratory experiments. Geophysical Journal International 157, 1393–1406.

25. Garel, F., Goes, S., Davies, D.R., Davies, J.H., Kramer, S.C., Wilson, C.R., 2014. Interaction of subducted slabs with the mantle transition-zone: A regime diagram from 2-D thermo-mechanical models with a mobile trench and an overriding plate. Geochem. Geophys. Geosyst., 15, 1739-1765, http://dx.doi.org/10.1002/2014GC005257.

26. Guillaume, B., Martinod, J., Espurt, N., 2009. Variations of slab dip and overriding plate tectonics during subduction: Insights from analogue modelling. Tectonophysics, 463, 167-174.

27. Guillaume, B., Funiciello, F., Faccenna, C., Martinod, J., Olivetti, V., 2010. Spreading pulses of the Tyrrhenian Sea during the narrowing of the Calabrian slab. Geology, 38, 9, 819–822.

28. Guillaume, B., Funiciello, F., Faccenna, C., 2021. Interplays between mantle flow and slab pull at subduction zones in 3D. Journal of Geophysical Research: Solid Earth, 126, e2020JB021574, 2021.

29. Haq, S.S.B., Davis, D.M., 2010, Mechanics of fore-arc slivers: Insights from simple analog models. Tectonics, 29. https:// doi .org /10 .1029 /2009TC002583.

30. Hervé, F., Fuentes, F., Calderón, M., Fanning, C.M., Quezada, P., Pankhurst, R., Rapela, C., 2017. Ultramafic rocks in the North Patagonian Andes: is their emplacement associated with the Neogene tectonics of the Liquiñe-Ofqui Fault Zone? Andean Geology, 44, 1, 1-16. doi: 10.5027/andgeoV44n1-a01.

31. Hervé, F., Pankhurst, R.J., Drake, R., Beck, M.E., 1995. Pillow metabasalts in a mid-Tertiary extensional basin adjacent to the Liquiñe-Ofqui fault zone: the Isla Magdalena area, Aysén, Chile. J. South Am. Earth Sci. 8, 33–46. doi:10.1016/0895-9811(94)00039-5.

32. Heuret, A., Funiciello, F., Faccenna, C., Lallemand, S., 2007. Plate kinematics, slab shape and back-arc stress: A comparison between laboratory models and current subduction zones. Earth and Planetary Science Letters, 256, 473–483.

33. Heyman J., 2019. TracTrac: A fast multi-object tracking algorithm for motion estimation. Computers & Geosciences, 128, 11-18. doi: 10.1016/j.cageo.2019.03.007

34. Jarrad, R.D., 1986a. Relations among subduction parameters. Review of Geophysics, 24, 2, 217-284.

35. Jarrad, R.D., 1986b. Terrane motion by strike-slip faulting of forearc slivers. Geology, 780-783.

36. Kimura, G., 1986. Oblique subduction and collision: forearc tectonics of the Kuril Arc. Geology, 14, 404-407.

37. Lallemand, S., Heuret, A., 2017. Subduction Zones Parameters. Reference Module in Earth Systems and Environmental Sciences. doi:10.1016/b978-0-12-409548-9.09495-1

38. Leever, K.A., Gabrielsen, R.H., Sokoutis, D., Willingshofer, E., 2011. The effect of convergence angle on the kinematic evolution of strain partitioning in transpressional brittle wedges: Insight from analog modeling and high-resolution digital image analysis. Tectonics, 30. https:// doi .org /10 .1029 /2010TC002823.

39. Li, C., van der Hilst, R.D., Engdahl, E.R., Burdick, S., 2008. A new global model for Pwave speed variations in Earth's mantle, Geochem. Geophys. Geosyst., 9, Q05018, doi:10.1029/2007GC001806.

40. Maffione, M., van Hinsbergen, D.J.J., Koornneef, L.M.T., Guilmette, C., Hodges, K., Borneman, N., Huang, W., Ding, L., Kapp, P., 2015. Forearc hyperextension dismembered the south Tibetan ophiolites. Geology, 43, 6, 475-478. doi:10.1130/G36472.1

41. Martinod, J., Funiciello, F., Faccena, C., Labanieh, S., Regard, V., 2005. Dynamical effects of subducting ridges: insights from 3-D laboratory models. Geophys. J. Int., 163, 1137–1150. doi: 10.1111/j.1365-246X.2005.02707.x

42. Martinod, J., Guillaume, B. Espurt, N., Faccena, C., Funiciello, F., Regard, V., 2013. Effect of aseismic ridge subduction on slab geometry and overriding plate deformation: Insights from analogue modeling. Tectonophysics, 588, 39-55.

43. McCaffrey, R., 1992. Plate convergence, slip vectors, and forearc deformation. Journal of Geophysical Research, 97, B6, 8905-8915.

44. Nakada, M., Okuno, J., Irie, Y., 2018. Inference of viscosity jump at 670 km depth and lower mantle viscosity structure from GIA observations, Geophysical Journal International, 212, 3, 2206–2225.Nelson, E., Forsythe, R., Arit, I., 1994. Ridge collision tectonics in terrane development. Journal of South America Earth Sciences, 7, 271–278.

45. Philippon, M., Corti, G., 2016. Obliquity along plate boundaries. Tectonophysics, 693(B), 171-182.

46. Ramsay, J., Huber, M., 1983. The Techniques of Modern Structural Geology. Volume 1: Strain Analysis. Academic Press, 307pp. San Diego.

47. Salze, M., Martinod, J., Guillaume, B., Kermarrec, J-J., Ghiglione, M., Sue, C., 2018. Trench-parallel spreading ridge subduction and its consequences for the geological evolution of the overriding plate: Insights from analogue models and comparison with the Neogene subduction beneath Patagonia. Tectonophysics, doi:10.1016/j.tecto.2018.04.018.

48. Schellart, W.P., 2005. Influence of the subducting plate velocity on the geometry of the slab and migration of the subduction hinge. Earth and Planetary Science Letters, 231, 197-219.

49. Schellart, W.P., Freeman, J., Stegman, D.R., Moresi, L., May, D., 2007, Evolution and diversity of subduction zones controlled by slab width. Nature, 446, 308–311. doi: 10.1038/nature05615.

50. Schellart, W.P., 2011. Rheology and density of glucose syrup and honey: determining their suitability for usage in analogue and fluid dynamic models of geological processes. J. Struct. Geol., 33, 1079–1088. http://dx.doi.org/10.1016/j.jsg.2011.03.013.

51. Steinberger, B., Calderwood, A.R., 2006. Models of large-scale viscous flow in the Earth's mantle with constraints from mineral physics and surface observations, Geophys. J. Int., 167, 1461-1481.

52. Suárez, R.J., Guillaume, B., Martinod, J., Ghiglione, M., Sue, C., Kermarrec, J-J., 2022. Experimental data of analogue models addressing the influence of oblique convergence and inheritance on sliver tectonics. GFZ Data Services. https://doi.org/10.5880/fidgeo.2022.013

53. Teyssier, C., Tikoff, B. Markley, M., 1995. Oblique plate motion and continental tectonics. Geology, 23, 5, 447-450.

54. Thielicke, W., 2014. The Flapping Flight of Birds - Analysis and Application. Phd thesis, Rijksuniversiteit Groningen, http://irs.ub.rug.nl/ppn/382783069

55. Thielicke, W., Stamhuis, E.J., 2014. PIVlab – Towards User-friendly, Affordable and Accurate Digital Particle Image Velocimetry in MATLAB. Journal of Open Research Software. DOI: http://dx.doi.org/10.5334/jors.bl

56. Thomson, S.N., 2002. Late Cenozoic geomorphic and tectonic evolution of the Patagonian Andes between latitudes 42°S and 46°S: An appraisal based on fission-track results from the transpressional intra-arc Liquiñe-Ofqui fault zone. GSA Bulletin, 114, 9, 1159–1173.

57. Tikoff, B., Teyssier, C., 1994. Strain modeling of displacement-field partitioning in transpressional orogens. Journal of Structural Geology, 16, 11, 1575-1588.

58. van der Meer, D.G., van Hinsbergen, D.J.J., Spakman, W., 2018. Atlas of the underworld: Slab remnants in the mantle, their sinking history, and a new outlook on lower mantle viscosity. Tectonophysics 723, 309-448. https://doi.org/10.1016/j.tecto.2017.10.004

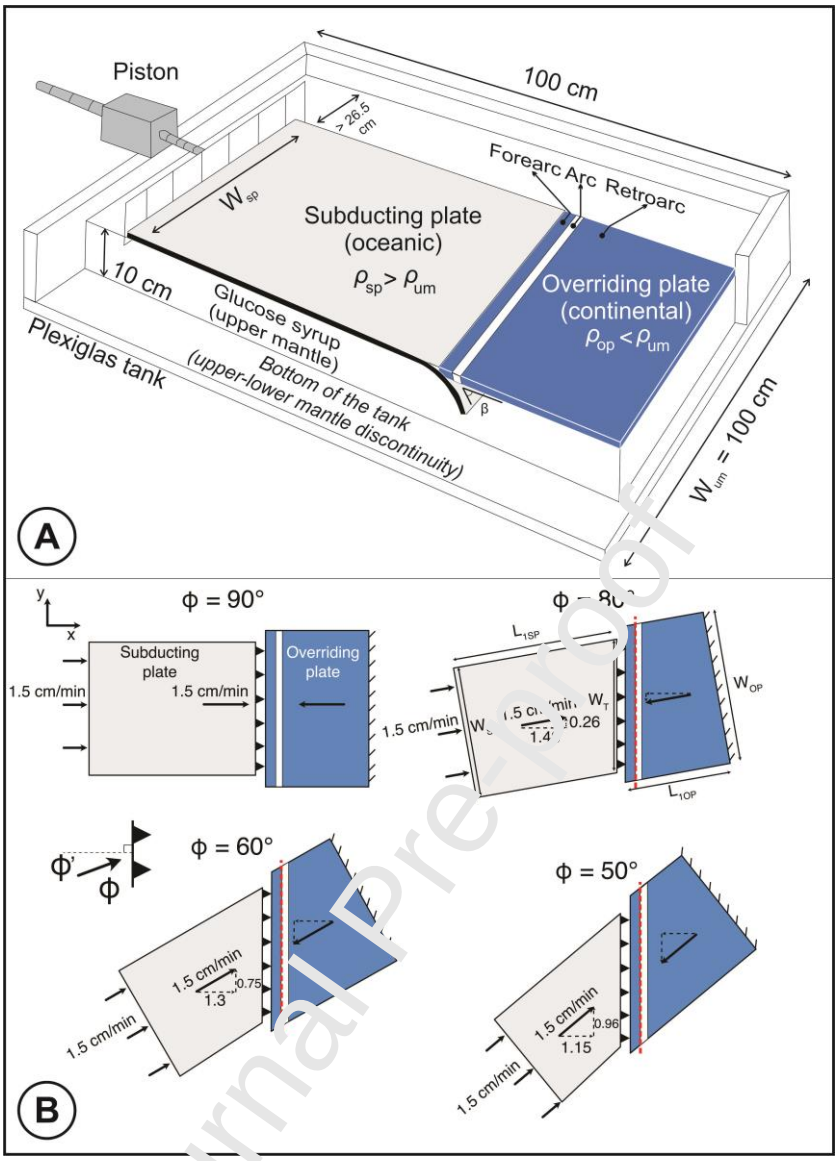

FIGURE 1. A) 3D-view of the experimental set-up. The arc is made of silicone whose viscosity is around 40% that of the rest of the overriding plate. ρ_{sp}= density of the subducting plate. ρ_{op}= density of the overriding plate. ρ_{um}= density of the sub-lithospheric upper mantle. W_{op}= width of the overriding plate. W_{sp}= width of the subducting plate. W_{um}= width of the sub-lithospheric upper mantle. **B)** Top-view of the geometry chosen for the subduction models with trench-oblique convergence angle. The red line indicates the position of the weak zone implemented in Model-05, Model-06, and Model-07.

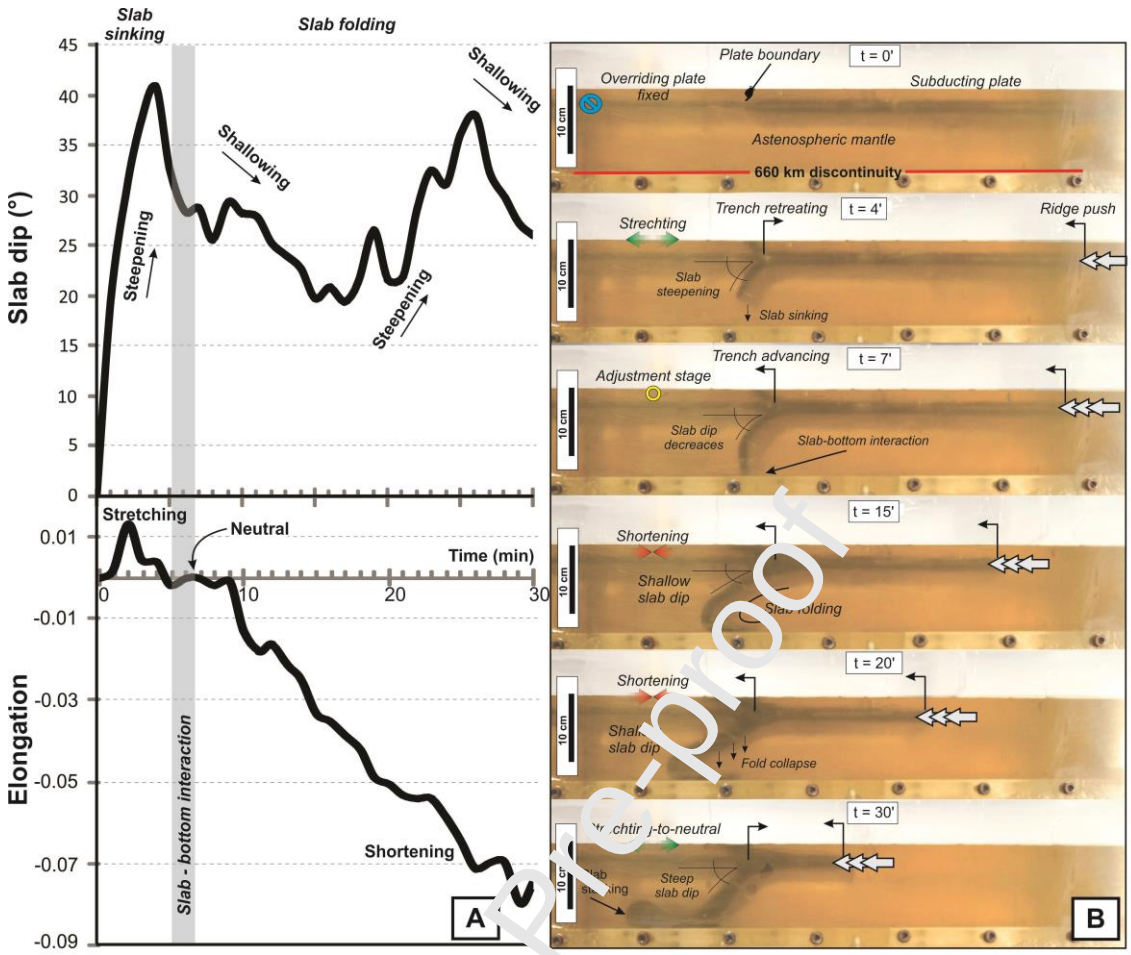

FIGURE 2. Slab dip evolution and its relationship with the convergence-parallel longitudinal strain of the overriding plate for the reference experiment (Model-01). **A)** Diagrams showing the time evolution of slab dip measured at 3-cm depth (top) and convergence parallel elongation measured in the center of the overriding plate (bottom). **B)** Lateral views of the experiment showing the slab geometry evolution. Periods of high slab dip are associated with stretching or moderate shortening of the overriding plate, while periods of low slab dip are associated with higher amounts of shortening.

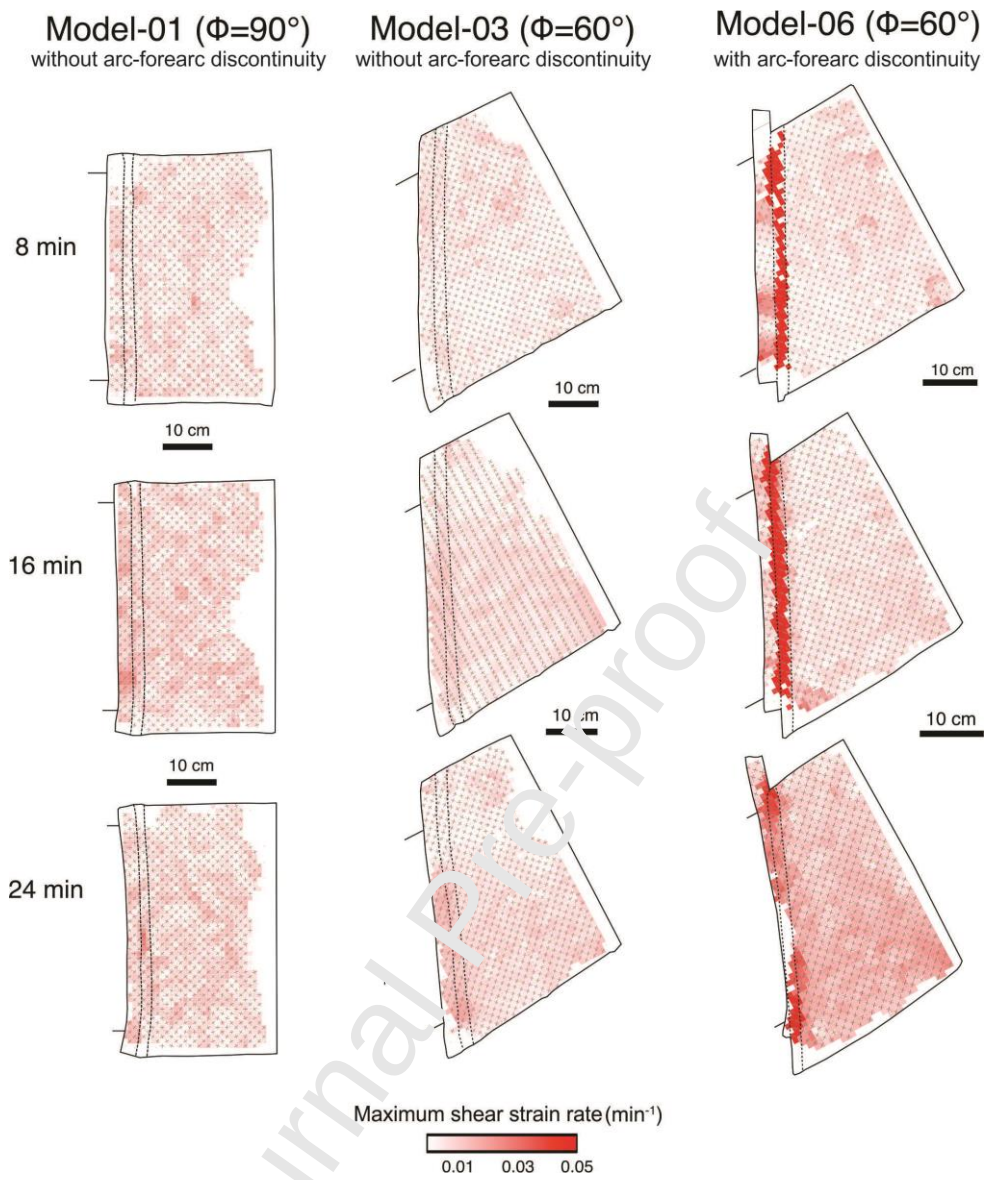

FIGURE 3. Instantaneous maximum shear strain rate at different times of the experiment for the reference model (Model-01) and for models with a trench-convergence angle of Φ= 60°. The same analysis for the rest of the experiments is presented in the **Supplementary Material 1**. All models are shown with an N-S oriented trench. The strain is computed from pictures taken with a 1-minute interval.

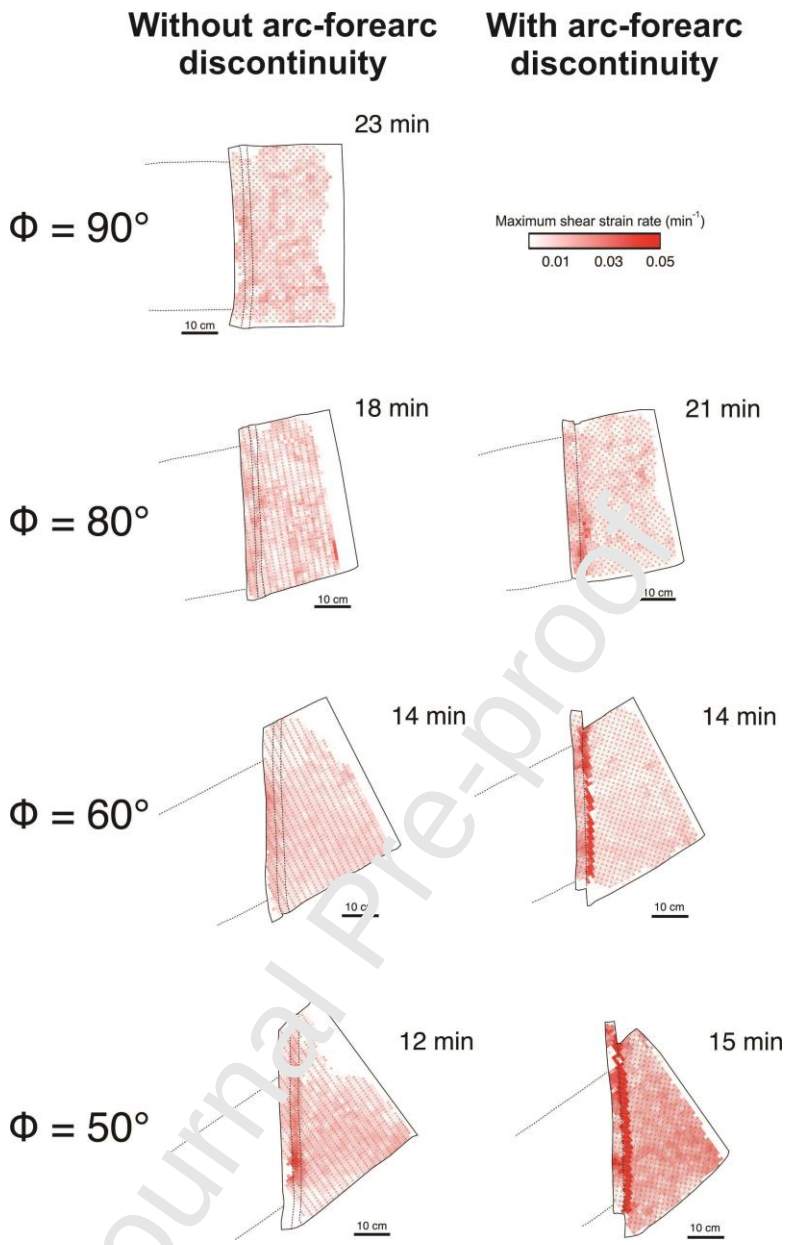

FIGURE 4. Instantaneous maximum shear strain rate in the overriding plate (top view) for the different models with variable obliquity computed after the slab has touched the bottom of the box, i.e., during slab folding. All models are shown with an N-S oriented trench. Strain is computed from pictures taken with a 1-minute interval.

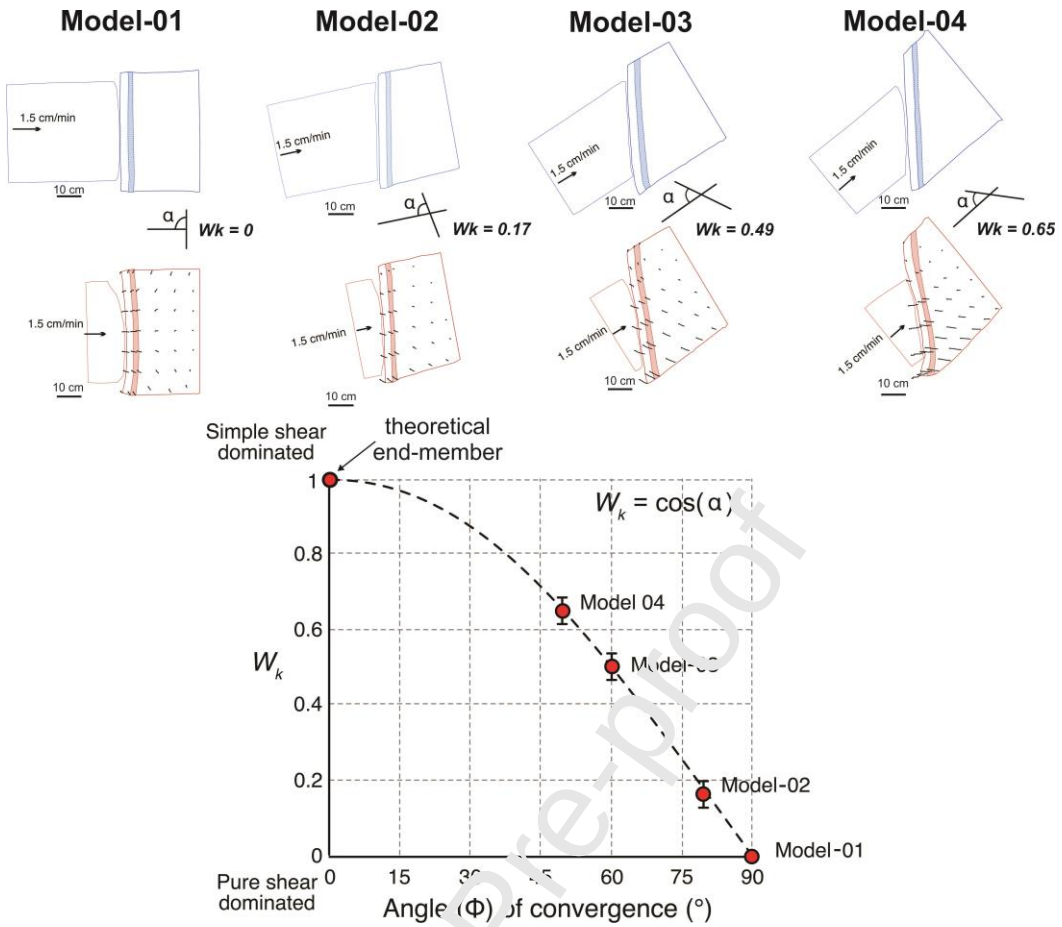

FIGURE 5. Initial (blue) and final (red) horizontal shapes of the subducting and overriding plates, and paths followed by individual particles for models with varying obliquity and no weak zone. The colored strip in the overriding plate corresponds to the arc position. In the lower diagram, the kinematic vorticity number *Wk* (red dots) is determined from the angle between flow apophyses and is displayed as a function of the angle of convergence (Φ). The value of Wk decreases as a function of the cosine of the angle of convergence (black dashed line) indicating that deformation at the plate scale shifts from pure-shear dominated to sub-simple shear when departing from trench-orthogonal convergence.

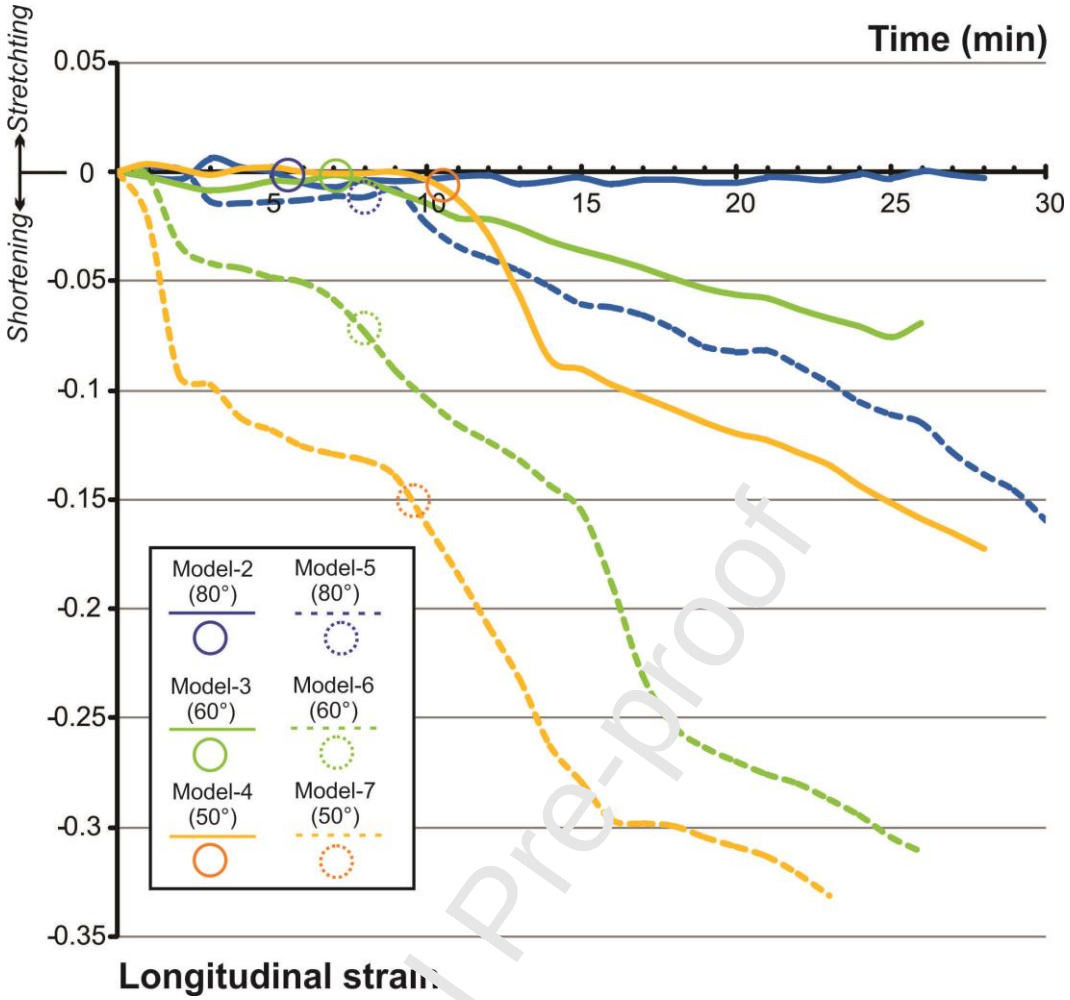

FIGURE 6. Time evolution of the longitudinal strain (convergence-parallel elongation, e) measured in the center of the overriding plate for models without (solid lines) and with (dashed lines) pre-existing fault. The measurements follow the equation $e = (lf - li)/li$, where lf is the final length and li the initial length. In this way, negative values indicate shortening. The circles indicate the time when the slab reaches the bottom of the box. Note that following slab interaction with the bottom of the box, the upper plate undergoes an abrupt increase in shortening whatever the obliquity of convergence.

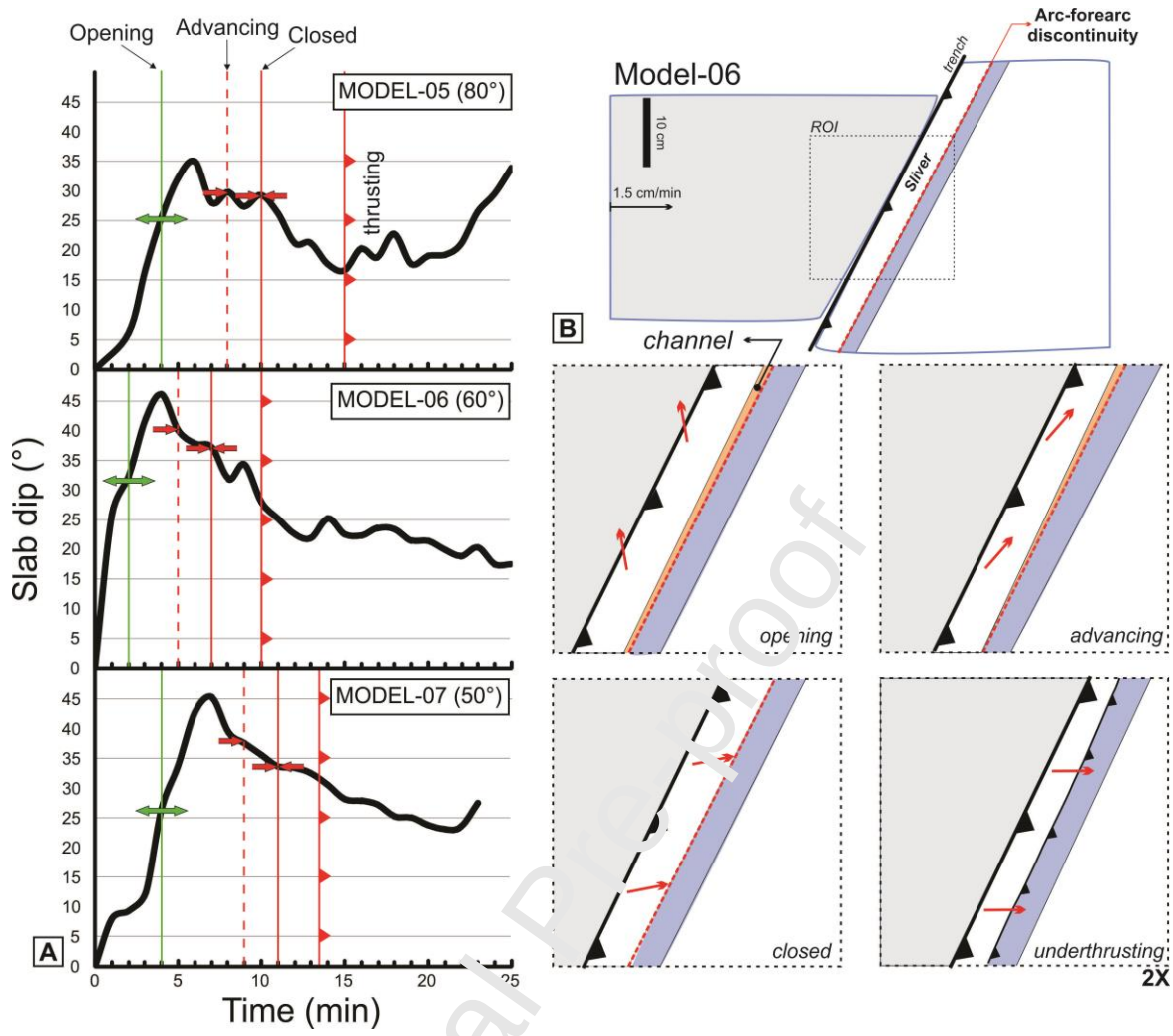

FIGURE 7. A) Slab dip evolution (measured at 3-cm depth at the edge of the slab) for the experiments with trench-oblique convergence and with arc-forearc discontinuity. The green line, red dashed line and red solid line indicate stages of channel opening between the arc and forearc, advancing motion of the sliver forearc, and full closure of the channel, respectively. The red solid line with triangles indicates the time in which the forearc is underthrusted by the arc. **B)** Schematic plan view of the different stages depicted in **A**, as example is used Model-06. The red arrows depict the relative motion of the sliver.

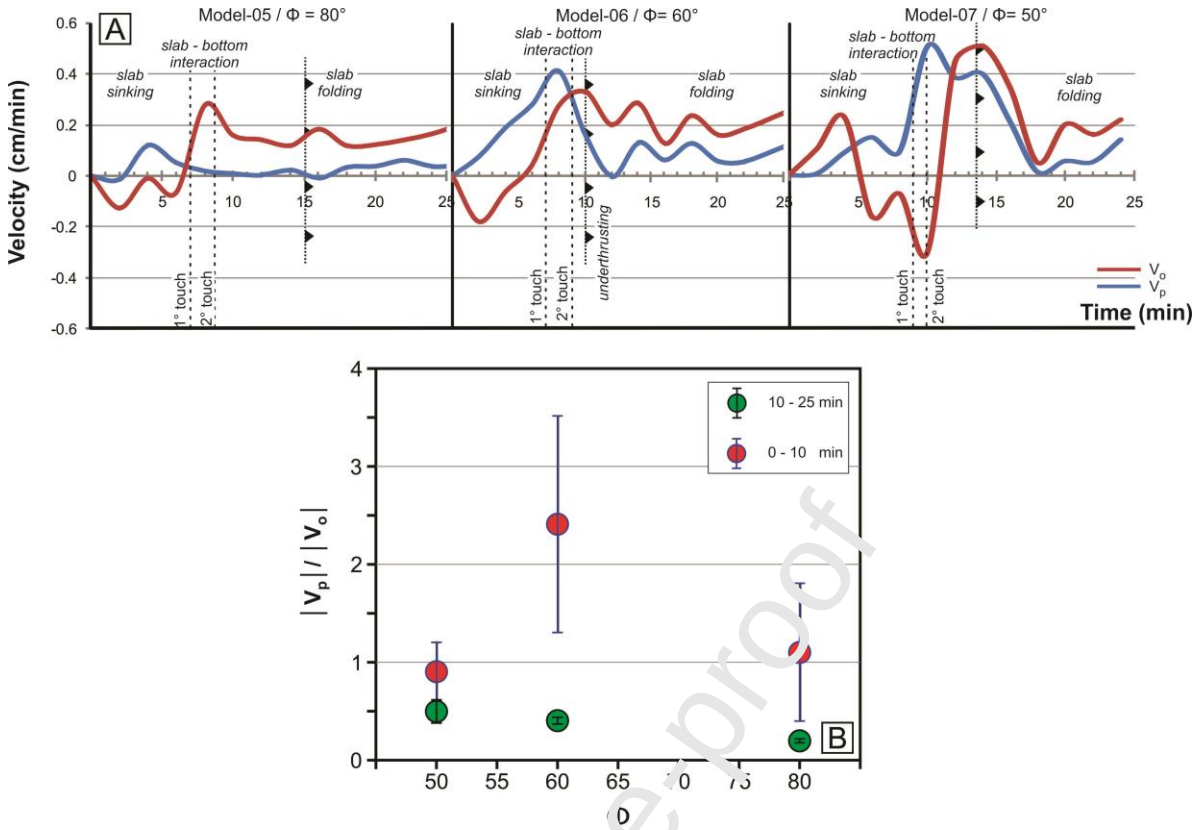

FIGURE 8. Kinematics of the sliver forearc. **A)** Time evolution of the trench-orthogonal (V_o, red line) and trench-parallel (V_p, blue line) components of the sliver velocity vector for different convergence obliquities: Φ = 80° (Model-05), Φ = 60° (Model-06), Φ = 50° (Model-07). The velocity is measured and averaged on a 4 cm x 3 cm area in the center of the forearc. First and second touches refer to the moment that the north and south sides of the slab reach the bottom of the tank, respectively. Negative values for V_o indicate oceanward motion of the forearc and negative values for V_p indicate a southward motion (i.e., sinistral strike-slip motion) of the forearc. **B)** V_p / V_o ratio averaged over two-time intervals (after and before the slab reaches the bottom of the tank) as a function of the convergence-trench angle (Φ).

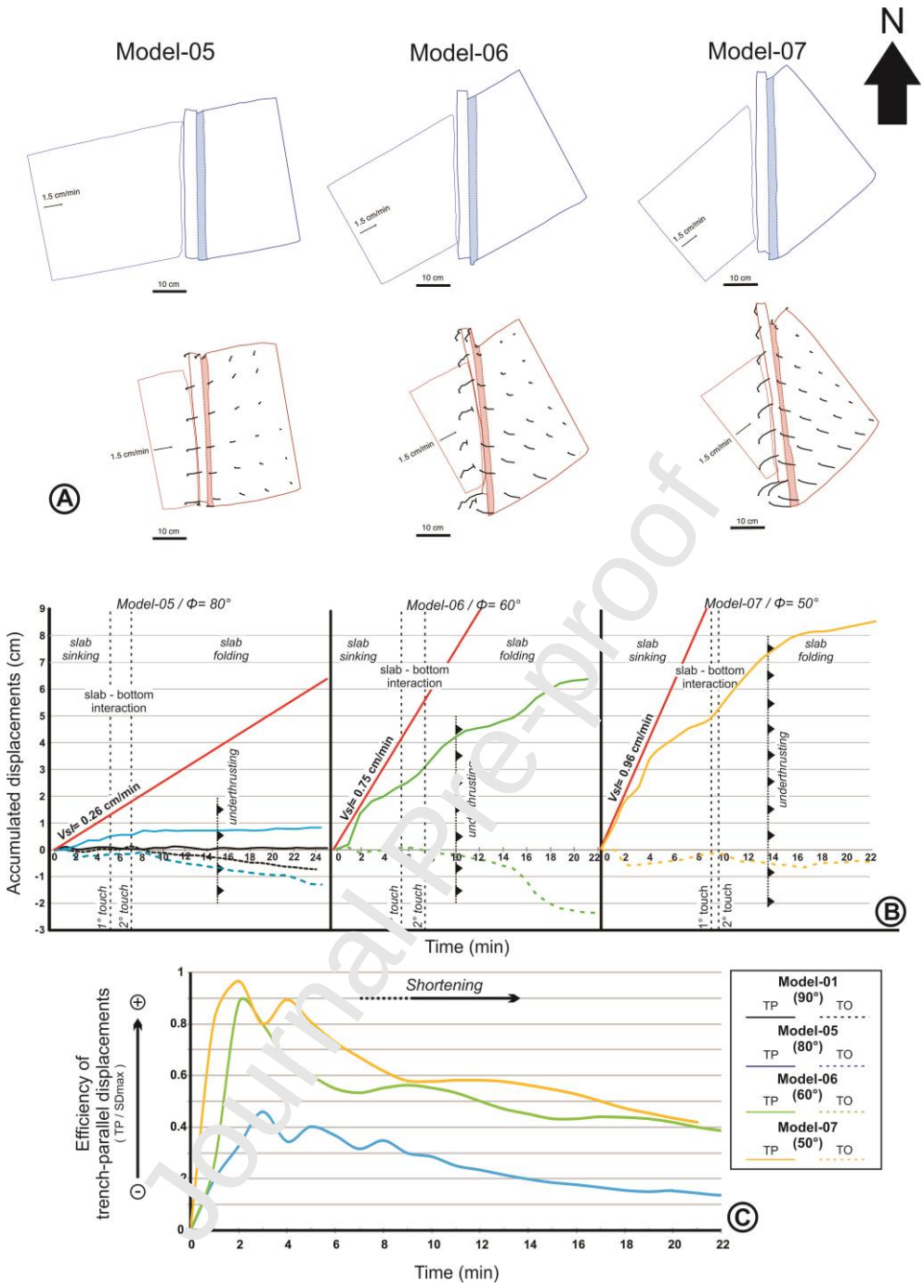

FIGURE 9. A) Initial and final horizontal shapes of the subducting and overriding plates, and paths followed by individual particles for models with varying obliquity and the presence of a pre-existing fault. The colored strip in the overriding plate corresponds to the arc position. Lines ending with a bar indicate that the portion of the forearc has been thrusted by the arc and that the points cannot be tracked anymore. **B)** Relative trench-parallel (TP, solid lines) and trench-orthogonal (TO,

dashed lines) accumulated displacements between pairs of points located in the forearc and retroarc domains, averaged among the northern, central, and southern sectors. The red lines indicate the maximum expected, trench-parallel component (Vsl_{max}), following the equation $Vc * \sin(90 - \Phi)$, where Vc is the convergence velocity and Φ the convergence angle (see geometrical meaning in figure 1B). For Model-05, we also show the values obtained in the central portion of the reference model (Model-01). **C)** Efficiency of the relative trench-parallel (TP) accumulated displacements for Model-05, Model-06, and Model-07, estimated as TP / sliver maximum accumulated displacements (SD_{max}). This graphic outlines the lower efficiency of sliver motion when shortening is ongoing.

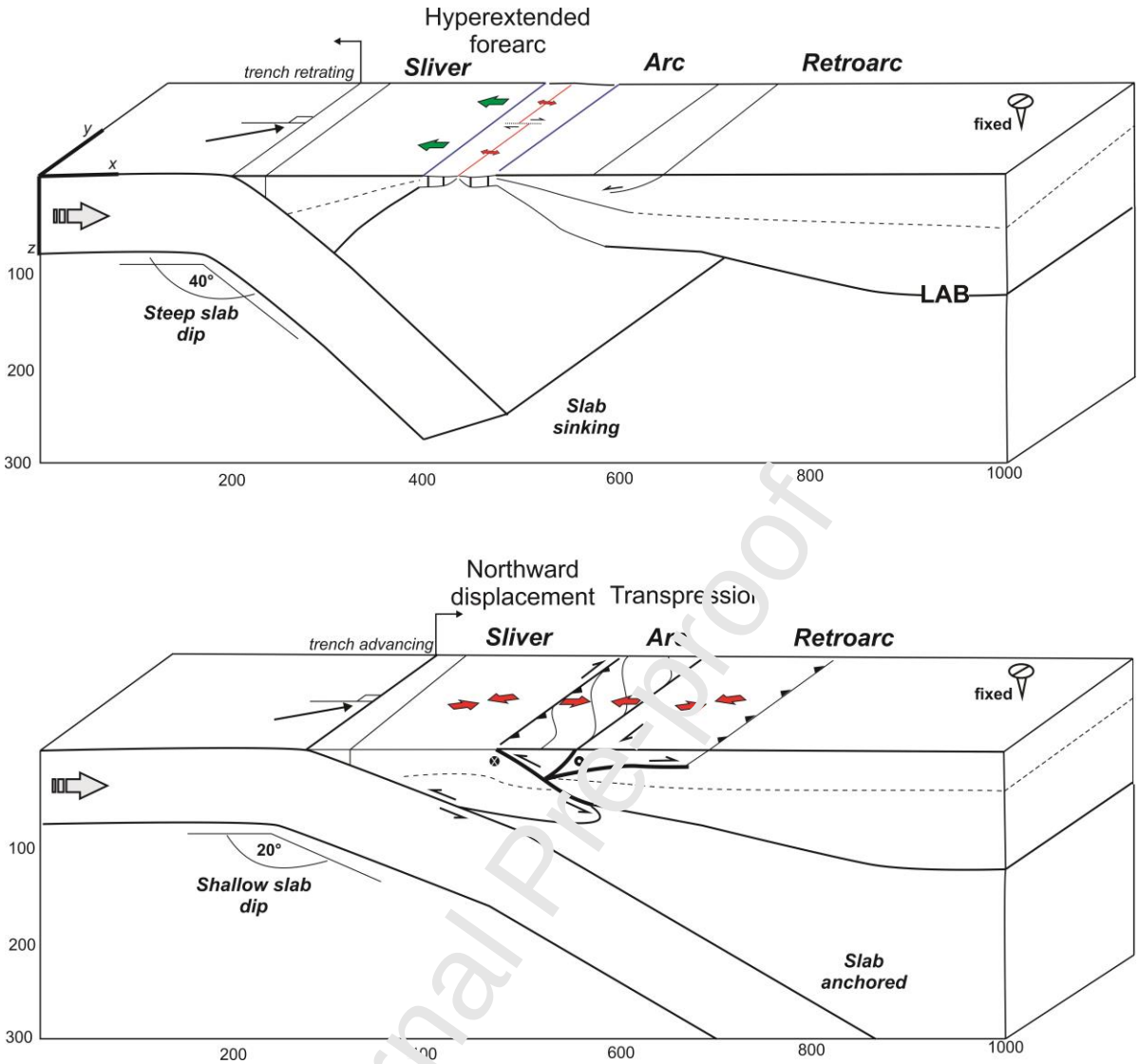

FIGURE 10. 3-D synoptic sketches illustrating the orogenic evolution of slivered margins. In this regard, the existence of a Sliver forearc may explain the development of hyperextended forearc regions, and subsequent forearc underthrusting, shaping in this way, a doubly-vergent orogenic architecture.

CONFLICT OF INTEREST STATEMENTS

The authors declare no known financial or personal interest conflict.

Rodrigo Suárez: *Conceptualization; Methodology; Formal analysis; Investigation; Writing - Original Draft*. **Guillaume Benjamin:** *Conceptualization; Methodology; Formal analysis; Investigation; Writing - Original Draft*. **Joseph Martinod:** *Methodology; Investigation; Writing - Original Draft*. **Matías Ghiglione:** *Writing - Review & Editing; Funding acquisition*. **Christian Sue:** *Writing - Review & Editing; Funding acquisition*. **Jean-Jacques Kermarrec:** *Methodology*.

HIGHLIGHTS

- We perform upper mantle-scale subduction experiments under laboratory conditions to assess the trench-oblique plate convergence.
- Some subduction experiments were modeled with a weak zone along the forearc-arc interface to investigate the role of inheritance on sliver tectonics.
- The strain across the overriding plate shift from pure-shear to sub-simple shear when convergence departs from orthogonal to oblique.
- Sliver tectonics only is developed when the overriding plate is embedded with a weak zone, simulating an inherited, lithospheric-scale fault.
- The experimental results yield new insights to evaluate the evolution of subduction-related orogens with sliver block.